



Proton-coupled electron transfer activation of peroxydisulfate with phosphorylated zero-valent iron

Chuan Liang^a, Xiufan Liu^b, Cancan Ling^c, Furong Guo^a, Meiqi Li^c, Xiang Zhang^a, Yiyi Shu^a, Hongwei Sun^{a,*}, Zhihui Ai^{a,*}, Lizhi Zhang^{a,c,**}

^a Key Laboratory of Pesticide & Chemical Biology of Ministry of Education, Institute of Environmental & Applied Chemistry, College of Chemistry, Central China Normal University, Wuhan 430079, PR China

^b Hubei Key Laboratory of Pollutant Analysis and Reuse Technology, College of Chemistry and Chemical Engineering, Hubei Normal University, Huangshi 435002, PR China

^c School of Environmental Science and Engineering, Shanghai Jiao Tong University, Shanghai 200240, PR China

ARTICLE INFO

Keywords:

Peroxydisulfate activation
Zero-valent iron
Proton-coupled electron transfer
Phosphate proton relays

ABSTRACT

Heterogeneous peroxydisulfate (PDS) activation driven by conventional electron transfer (ET) is often frustrated by low thermodynamic driving force and sluggish kinetics. Herein, we propose a proton-coupled electron transfer (PCET) strategy of PDS activation, by utilizing ball-milled phosphorylated zero-valent iron (P-ZVI^{bm}) as a PCET platform. P-ZVI^{bm} efficiently activated PDS to produce SO₄^{•-} and •OH for rapid degradation of 4-chlorophenol in a wide pH range of 3.5–10.5, with rate constants 3–62 times those of the ZVI^{bm}/PDS counterpart. PCET mechanism was evidenced by the pH dependent kinetics, kinetic isotope effect, and proton inventory study. The surface-bound phosphates offer flexible pendant protons (P-O-H) through hydrogen bonds, delocalizing electrons of peroxide O to polarize the O-O bond, thereby facilitating the ET from ZVI for O-O bond cleavage. The work demonstrates the superiority of PCET strategy for heterogeneous PDS activation, and shall guide the design of high-performance Fenton-like catalysts.

1. Introduction

Advanced oxidation processes (AOPs) are powerful water purification technologies to destroy refractory organic pollutants by generating highly reactive oxygen species (ROs), commonly arisen from activation of oxidants such as hydrogen peroxide (H₂O₂), peroxymonosulfate (HSO₅⁻, PMS) and peroxydisulfate (S₂O₈²⁻, PDS) [1–4]. As an appealing solid oxidant, PDS is standout by virtue of its low cost (0.18 \$ mol⁻¹ versus 1.36 \$ mol⁻¹ for PMS and 0.05 \$ mol⁻¹ for H₂O₂), better chemical stability during storage (months versus hours to days for PMS or H₂O₂), and safer handling than liquid H₂O₂ [5,6]. PDS produces strong oxidizing sulfate radicals (SO₄^{•-}, E° = 2.6 ~ 3.1 V vs NHE) through O-O bond cleavage, driven either by energy transfer (e.g., heat, UV, ultrasound), or by electron transfer (ET) in the presence of activators such as transition metal ions and metal oxides [7,8]. The energy transfer methods were not applicable for large-scale sites such as groundwater remediation due to the cost and technique limitations. The ET route of

PDS activation, especially with heterogeneous catalysts, is more appealing currently because of its lower cost and environmental benignancy. However, despite the lower O-O bond energy of PDS (92 kJ mol⁻¹ versus 377 kJ mol⁻¹ of PMS), the heterogeneous PDS activation reactions generally possess slower kinetics than the PMS counterparts [6,9,10]. One primary reason is the symmetric structure of PDS, with each -SO₃ moiety on both sides of the O-O bond. Asymmetric PMS can adsorb on the surface of heterogeneous electron donors by the O-O-H terminal, with the peroxide O atom in the first coordination sphere of transition metals, which facilitates the inner sphere ET from metal to the O-O bond [11]. Whereas the steric hinderance of two -SO₃ disfavors such a sorption pattern of PDS, but instead prefers the -SO₃ end-on coordination mode, where the transition metal and the peroxide O are bridged by the -SO₃ moiety, resulting in great increase of the ET distance. According to the Marcus theory of ET, the longer distance between electron donor and acceptor shall decrease the electron coupling constant (V_{el}), thus significantly frustrating the kinetics of ET

* Corresponding authors.

** Corresponding author at: Key Laboratory of Pesticide & Chemical Biology of Ministry of Education, Institute of Environmental & Applied Chemistry, College of Chemistry, Central China Normal University, Wuhan 430079, PR China.

E-mail addresses: sunhw@mail.ccnu.edu.cn (H. Sun), jennifer.ai@mail.ccnu.edu.cn (Z. Ai), zhanglz@mail.ccnu.edu.cn (L. Zhang).

<https://doi.org/10.1016/j.apcatb.2024.124025>

Received 14 February 2024; Received in revised form 22 March 2024; Accepted 1 April 2024

Available online 1 April 2024

0926-3373/© 2024 Elsevier B.V. All rights reserved.

for the lysis of O-O bond (Eq.1)^[a] [12]. Meanwhile, the inherently nonpolar and negative charged O-O bond of PDS are also adverse to the ET activation. Therefore, developing a novel avenue to boost the PDS activation is of great significance but still challenging.

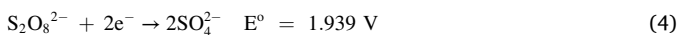
$$k_{ET} = \frac{|V_{el}|^2}{h} \sqrt{\frac{\pi}{4\lambda k_B T}} \exp \left[\frac{-(\Delta G_{ET}^0 + \lambda)^2}{4\lambda k_B T} \right] \quad (1)$$

[a] Eq. 1 is the semi-classical, high-temperature expression for the rate constant of non-adiabatic electron transfer (k_{ET}) as a function of electronic coupling (V_{el}), reorganization energy (λ), and reaction Gibbs free energy (ΔG_{ET}^0). h is the Planck constant, k_B is the Boltzmann's constant, and T is the temperature.

Proton-coupled electron transfer (PCET) processes could often possess energetic advantages over the sole ET processes, because the positive protons and negative electrons are attracted to each other and contribute to the electrostatic stabilization of the reaction system [12–15]. Moreover, the coupled transfer of proton and electron avoids the high-energy intermediates of single ET, affording larger driving force and lower activation barrier in many chemical and biochemical reactions [13,16]. So far, researchers have utilized the nature of PCET pathways to benefit numerous catalytic systems including electrochemical hydrogen evolution and oxygen reduction reactions, both thermodynamically and kinetically [12,17–19]. To the best of our knowledge, PCET processes are never applied for the PDS activation previously, although the electrochemical reductive O-O cleavage of organic peroxides could be driven in a PCET pathway [20]. Given the similar target O-O structure between PDS and organic peroxides, we propose that the PCET mechanism might promote the O-O bond activation of PDS.

To validate this hypothesis, we theoretically compared the Gibbs free energy change (ΔG^0) of sole ET and PCET activation of PDS, because more negative ΔG^0 would result in lower Eyring barrier (ΔG^\ddagger) according to the Marcus equation (Eq.2) [21]. The approximate estimates are made in the case of considering PDS activating half reactions. First, the Gibbs free energy change during the sole ET process (ΔG_{ET}^0 , Eq.3) can be obtained as follows. Given the standard reduction potentials (E^0) of $S_2O_8^{2-}$ (Eq.4) and $SO_4^{\bullet-}$ (Eq.5) [22], their free energy changes (ΔG_4^0 and ΔG_5^0) are calculated according to Eq.6, with ΔG_4^0 of $-374.2 \text{ kJ mol}^{-1}$ and ΔG_5^0 in the range from $-241.2 \text{ kJ mol}^{-1}$ to $-299.1 \text{ kJ mol}^{-1}$, respectively. $\Delta G_{ET}^0 = \Delta G_4^0 - \Delta G_5^0$, ranges from $-133.0 \text{ kJ mol}^{-1}$ to $-75.1 \text{ kJ mol}^{-1}$. The PCET activation of PDS shall follow the patterns of Figure S1, where the free energy change of PCET pathway (ΔG_{PCET}^0) equals the summation of ΔG_{ET}^0 and ΔG_{PT}^0 (PT represents proton transfer) based on the features of thermodynamic state functions [23]. The free energy change of the PT process ($\Delta G_{PT}^0 = -11.4 \text{ kJ mol}^{-1}$) is obtained from the acid dissociation constant of HSO_4^- ($pK_a = 1.99$) following Eq.7 [24]. Thus $\Delta G_{PCET}^0 = \Delta G_{ET}^0 + \Delta G_{PT}^0$, i.e., in the range of $(-144.4) \sim (-86.5) \text{ kJ mol}^{-1}$, which is obviously more negative than ΔG_{ET}^0 , resulting in lower Eyring barrier (ΔG^\ddagger), i.e., the change of Gibbs free energy from reactants to the transition state. Therefore, the PCET pathway might enhance the thermochemical driving force of the PDS activating reaction, and then increase the kinetic rate constant k , following the Eyring equation (Eq.8). The above results reveal that the PCET route might be a promising strategy to promote the PDS activation.

$$\Delta G^\ddagger = \frac{\lambda}{4} \left(1 + \frac{\Delta G^0}{\lambda} \right)^2 \quad (2)$$



$$\Delta G^0 = -zFE^0 \quad (6)$$

$$\Delta G_{PT}^0 = RT \ln(K_a) = -2.303RT(pK_a) \quad (7)$$

$$k = \frac{k_B T}{h} \exp \left(\frac{-\Delta G^\ddagger}{RT} \right) \quad (8)$$

Since the PCET mechanism requires the transfer of both electron and proton to the O-O bond of PDS, the PCET activation of PDS requires a platform with both electron and proton inventories. Zero-valent iron (ZVI) is a popular electron donor for the activation of PDS, owing to the advantages such as easy-access, inexpensiveness, and eco-benignancy [25,26]. Moreover, water often serves as the final proton donor of the PCET reactions conducted in the aqueous solution, usually with the aid of proton relays, which gain protons from water and subsequently donate these protons to final acceptors [19]. Phosphate, with moderate protonation capacity and strong interionic hydrogen bond forming potential, has been utilized as proton relays in many aquatic reactions [27]. These facts enlight us to build up an elaborate PCET platform for the activation of PDS, by integrating the electron donor ZVI and the proton relay phosphate in aquatic reactions. Fortunately, phosphate has intrinsic high affinity for iron species, making it facile to anchor the phosphate proton relay on the surface of ZVI through coordination [25]. More importantly, polyprotic phosphates may leave over the ZVI surface pendant acid-base residuals, which are flexible and may easily approach the peroxide O atom of the adjacently adsorbed PDS molecules for better proton transfer [28]. It is worth noting that phosphate or organic acids have been employed as efficient proton transmitters in Fe⁰-based Fenton-like processes, whose roles mostly focus on the formation of $\bullet H$ which promotes O_2 activation to produce H_2O_2 through single electron transfer pathway [29,30], or to indirectly promote the generation of Fe (II) as electron donors [31,32]. Nevertheless, whether phosphate group can directly participate in boosting electron transfer to break the O-O bond and realize PCET activation of PDS at the interface, is still unclear.

Accordingly, we herein for the first time fabricated phosphorylated ZVI (P-ZVI^{bm}) through the simple ball-milling method as a paradigm of PCET platform to activate PDS in water, and then checked its performance to produce $SO_4^{\bullet-}$ for the degradation of various organic pollutants. The PCET mechanism of PDS activation was verified by investigating the pH-dependence and isotope effects of the PDS activating kinetics. Electrochemical proton inventory studies, spectroscopic characterization, and theoretical calculation were performed to reveal the PCET-associated interfacial processes and activation mechanism.

2. Materials and methods

2.1. Chemicals and reagents

All chemicals and reagents that were used in this study is available in Text S1 in the Supporting Information.

2.2. Preparation of P-ZVI^{bm}

P-ZVI^{bm} was prepared by mechanical milling method using commercial mZVI power (100 mesh) and K_3PO_4 as modifiers. Typically, 4.0 g of pristine mZVI was mixed with 0.15 g K_3PO_4 with P: Fe molar ratio of 0.01. The milling was carried out in a planetary ball mill (Chi Shun Technology Development Co., Ltd, Nanjing, China) with vacuum-sealed stainless steel jars (100 mL) containing 50 balls with a diameter of 6 mm and 20 balls with a diameter of 10 mm. The milling was performed at 500 rpm in a closed system at room temperature. A forward rotation and a reverse rotation milling were alternately carried out every 1 h. After 4 h of ball-milling process, the obtained black powder noted as P-ZVI^{bm} dried in a vacuum oven at 30 °C for 12 h and then stored in the vacuum bag to avoid further oxidation in the air. For comparison, ZVI^{bm} was prepared with the same procedure without K_3PO_4 addition.

2.3. Analytical methods

The 4-chlorophenol (4-CP) removal experiments were conducted in conical flasks (50 mL) in a shaker with a speed of 200 rpm at room temperature, with operation details presented in Text S3. The concentrations of the 4-CP were determined by the high-performance liquid chromatography, with detection details presented in Text S4. The durability of P-ZVI^{bm} was evaluated by recycling the used catalysts through filtration and washing with deionized water and dried at 30 °C in a vacuum oven for further use. The concentration of phosphorus was detected using the inductively coupled plasma mass spectrometry (ICP-MS) on Spectro Blue Sop. The reactive radicals were identified by Electron paramagnetic resonance using DMPO as the spin trapping agent. Kinetic isotope effect (KIE) experiments were performed in D₂O solution to obtain insight into the role of proton transfer during the PDS activation. The electrochemical proton inventory studies were

conducted by linear sweep voltammetry (LSV) measurements, with operation details presented in Text S5. Electrochemical PDS activation experiments with phosphorylated Fe sheet cathode were displayed in Text S6. The interactions between PDS and samples were examined by time-resolved *in-situ* attenuated total reflectance Fourier transform infrared (ATR-FTIR) spectra, where the recorded spectra were employed to conduct 2D correlation calculation using the software 2D Shige ver.1.3, with details showed in Text S7.

3. Results and discussion

3.1. Reactivity of P-ZVI^{bm} and activation pathways of PDS

The effect of ball-milling phosphate modification of ZVI on the PDS catalytic performance was first assessed by 4-chlorophenol (4-CP) degradation. Within 60 min, only approximately 9.1% of 4-CP was

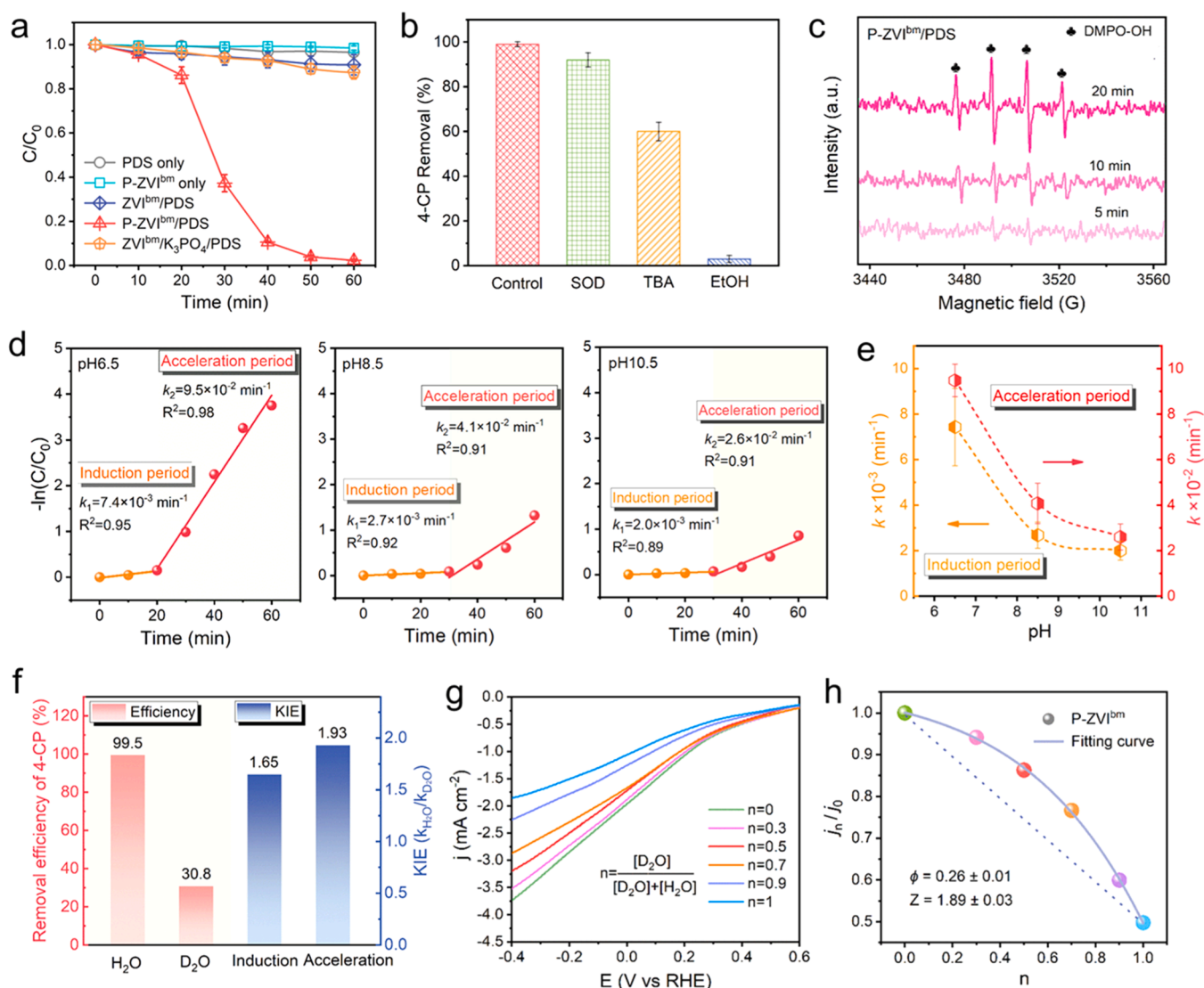
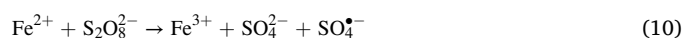


Fig. 1. Reactivity of P-ZVI^{bm} and activation pathways of PDS. (a) Time profiles of 4-CP removal in different systems. Reaction conditions: [4-CP]₀ = 0.1 mmol L⁻¹, [PDS]₀ = 1 mmol L⁻¹, [P-ZVI^{bm}] = [ZVI^{bm}] = 0.2 g L⁻¹, [K₃PO₄] = 0.38 mmol L⁻¹, initial pH (pH_{ini}) = 6.5 (if not specified). (b) Degradation efficiency of 4-CP in P-ZVI^{bm}/PDS system with different scavengers. Reaction conditions: [SOD]₀ = 100 mg L⁻¹, [TBA]₀ = [EtOH]₀ = 200 mmol L⁻¹. (c) EPR signals of P-ZVI^{bm}/PDS using DMPO as the trapping agent over time. Reaction conditions: [DMPO]₀ = 100 mmol L⁻¹. (d) Plots of $-\ln(C/C_0)$ versus time for 4-CP degradation for the induction and acceleration period of P-ZVI^{bm}/PDS at different pH. (e) Plots of reaction rate constant as a function of the initial pH value. (f) The degradation efficiency of 4-CP by P-ZVI^{bm} in H₂O and D₂O, respectively, and the calculated KIE of D₂O for the induction and acceleration period of P-ZVI^{bm}/PDS, respectively. (g) LSV of the P-ZVI^{bm} electrode in the mixed electrolyte of H₂O and/or D₂O containing 1 mmol L⁻¹ PDS, and n is the atomic deuteration fractions. (h) Plots of j_n/j_0 as a function of n for the P-ZVI^{bm}, where j_n and j_0 represents the current density obtained in the electrolyte with a specific atomic deuteration fractions n and in the only protonic electrolyte, respectively.

degraded in the ball-milled ZVI activated PDS system (ZVI^{bm}/PDS), whereas 97.6% of 4-CP was removed in the ball-milled phosphorylated ZVI activated PDS system (P-ZVI^{bm}/PDS) (Fig. 1a). PDS or P-ZVI^{bm} alone had little effect on the 4-CP degradation. Besides, the addition of equivalent K₃PO₄ to ZVI^{bm}/PDS (ZVI^{bm}/K₃PO₄/PDS) only removed 12.6% of 4-CP, indicating the indispensability of P-ZVI^{bm} to the high-performance PDS activation, while the promotion effect of PO₄^{3−} on the PDS activation of ZVI could be attributed to the surface-bound anions. Moreover, the key role of the possible generated FePO₄ or Fe₃(PO₄)₂ on the surface had been ruled out, with details shown in Figure S2. Regarding that the specific surface area (SSA) of P-ZVI^{bm} (0.48 m² g^{−1}) was slightly larger than that of ZVI^{bm} (0.18 m² g^{−1}) (Figure S3a, b), we prepared ZVI^{bm} samples with different SSA (0.18, 0.63, 2.04 m² g^{−1}) by prolonging the ball milling time to 4, 8, 12 h, and found these ZVI^{bm} samples exhibited similarly poor performances, suggesting the outstanding activity of P-ZVI^{bm} could not be assigned to the increased SSA but the PO₄^{3−} modification (Figure S3c). Moreover, negligible phosphorus leached in the P-ZVI^{bm}/PDS system ruled out possible secondary pollution (0.0053 mg L^{−1}, Figure S4). Impressively, P-ZVI^{bm} also possessed excellent reusability, with 92.3% of 4-CP degradation even after five consecutive cycles of use (Figure S5).

The reactive species responsible for 4-CP degradation in the P-ZVI^{bm}/PDS system was then identified by quenching experiments. As shown in Fig. 1b, superoxide dismutase (SOD, scavenger of •O₂[−]) only slightly suppressed the degradation of 4-CP, while tert-butanol (TBA, scavenger of •OH) and especially ethanol (EtOH, scavengers of both •OH and SO₄^{•−}) significantly inhibited the 4-CP removal, suggesting that P-ZVI^{bm} followed the radical regime in the activation of PDS through lysis of the O-O bond. The DMPO trapped electron paramagnetic resonance (EPR) tests further verified the generation of radicals. The DMPO-OH signals were detected and gradually strengthened over time (Fig. 1c), while the DMPO-SO₄^{•−} signals were not observed, possibly due to its rapid hydrolysis to DMPO-OH [33,34]. Moreover, the 4-CP degradation pathway was proposed according to the determination results of intermediate products by GC-MS, which also confirmed the radical regime (Table S1 and Figure S6). The radical activation mechanism of the P-ZVI^{bm}/PDS system demonstrated that phosphate modification played an important role in the electron transfer from ZVI to PDS for the O-O bond lysis.

To check if phosphate modification promoted PDS activation through the PCET pathway, the influence of proton concentrations on the kinetics of P-ZVI^{bm}/PDS was investigated because the PCET process was closely related to proton participation. It was found that the initial solution pH strongly affected both the 4-CP degradation and the PDS decomposition (Figure S7 and Figure S8). ZVI^{bm} could only activate PDS at pH 3.5, which was attributed to the leaching of Fe²⁺ and the homogeneous PDS activation (Eq. 9 and eq. 10, Figure S9). In contrast, P-ZVI^{bm} was able to activate PDS in the wide pH range of 3.5–10.5, with the negligible Fe²⁺ leaching except for pH 3.5, suggesting the dominant heterogeneous PDS activation in the P-ZVI^{bm}/PDS systems at neutral and alkaline conditions. Intriguingly, both the PDS decomposition and the 4-CP removal profiles of P-ZVI^{bm}/PDS showed two distinct phases including the initial induction period and the following acceleration period. To give a clear comparison of these two periods, 4-CP removal kinetics was fitted by the first-order reaction. As shown in Fig. 1d, the apparent rate constant of the induction period (*k*₁) gradually decreased with the increasing pH, with the prolonged duration. Then came the acceleration period where the apparent rate constant (*k*₂) also obviously declined with pH increasing. Thus, the 4-CP removal reaction kinetics in P-ZVI^{bm}/PDS was significantly pH-dependent (Fig. 1e and Table S2), implying the involvement of solution protons and the possible PCET reaction.



To provide more solid and direct proofs for the PCET process in the P-ZVI^{bm}/PDS system, the KIE experiment was explored with D₂O as the solvent instead of H₂O. The KIE experiments have been commonly accepted as an indicator of the PCET process because the heavier isotopes generally produce more stable chemical bonds and required greater activation energy to achieve the transition state, thus the substitution of proton (H) with deuterium (D) could significantly reduce the reaction rates when the solvent protons are involved in the rate-determining steps [35]. According to Fig. 1f, the 4-CP degradation efficiency of P-ZVI^{bm}/PDS decreased remarkably from 99.5% to 30.8% in D₂O, and the KIE values of the induction and acceleration phases were 1.65 and 1.93, respectively. Such substantial KIE values revealed the key roles of solvent protons and the prominent PCET process in the P-ZVI^{bm}/PDS system.

Because of very low proton concentration in the neutral and alkaline solutions, effective PCET activation usually requires that the activator have both electron donor sites and proton exchange sites. To further verify that the surface of P-ZVI^{bm} could deliver solution protons to the final PDS acceptors, electrochemical proton inventory studies were performed via LSV method. The electrochemical reaction rates attenuated with the increased atom fractions of deuterium (*n* = 0, 0.3, 0.5, 0.7 and 0.9) in the electrolyte, following a modified Gross-Butler equation (Eq. 11), where *j_n* and *j₀* were the current densities obtained with the atomic deuteration fractions of *n* and 0, respectively; *φ* was the isotopic fractionation factor; *Z* described the aggregate isotope effect of multiple equivalent hydrogenic sites (*Z*-sites), *Z* > 1 suggested the inverse isotope effect of the *Z*-sites on the catalytic kinetics, whereas *Z* = 1 indicated no contribution of the *Z*-sites to the kinetics [36,37]. As shown in Fig. 1g, the *j_n* of P-ZVI^{bm}/PDS system decreased gradually with the increase of *n*, and the *j_n*/*j₀*-*n* plot displayed a non-linear dome shape (Fig. 1h), with the *Z* value of 1.89 ± 0.03, indicating the inverse aggregate isotope effect of the *Z*-sites on the surface of P-ZVI^{bm}. In contrast, the *j_n*/*j₀*-*n* plot of the ZVI^{bm}/PDS system was linear with *Z* value of 0.86 ± 0.14 (Figure S10). Hence, the proton inventory studies offered solid evidence of the proton relay effect of the P-ZVI^{bm} surface during the PDS activation in the PCET pathway.

$$j_n = j_0 (1 - n + n\phi)^Z \quad (11)$$

3.2. Key active sites of PDS activation

The above experiments demonstrated the enhanced activation of the P-ZVI^{bm}/PDS system was attributed to the PCET reaction pathway. To gain a deep insight into this P-ZVI^{bm}-induced PCET activation of PDS, we carefully characterized the PCET platform P-ZVI^{bm} and the ZVI^{bm} counterpart to find out the key active sites. Scanning electron microscopy (SEM) and granulometric analysis revealed that the mechanochemical effect of the ball milling process significantly reduced the size of ZVI particles to get finer irregular particles (Figure S11 and Figure S12). The phosphate modification on the P-ZVI^{bm} surface was evidenced by the uniformly distributed P signals in the energy dispersive X-ray spectrometry (EDS) images (Fig. 2a), where the P element accounted for only 0.63 at% of the surface atoms (Figure S13). Notably, P-ZVI^{bm} still maintained the identical α-Fe phase bulk structure of ZVI according to the XRD patterns (Fig. 2b) and the similar sextet component with isomer parameter (*δ* = 0.12 mm s^{−1}) in the Mössbauer spectroscopy (Fig. 2c) [38]. Nevertheless, the reversed quadrupole shift (QS) parameter between ZVI^{bm} (QS = 0.01) and P-ZVI^{bm} (QS = −0.01) represented the subtle transformation of charge distribution symmetry of Fe nucleus, implying the distinct Fe coordination environments after phosphate modification [39]. The spatial distributions of P in the bulk phase of samples were then probed by time-of-flight secondary ion mass spectroscopy (ToF-SIMS) depth profile with Cs⁺ sputtering (Fig. 2d). ZVI^{bm} only displayed very weak P⁺ signal owing to the noise of the

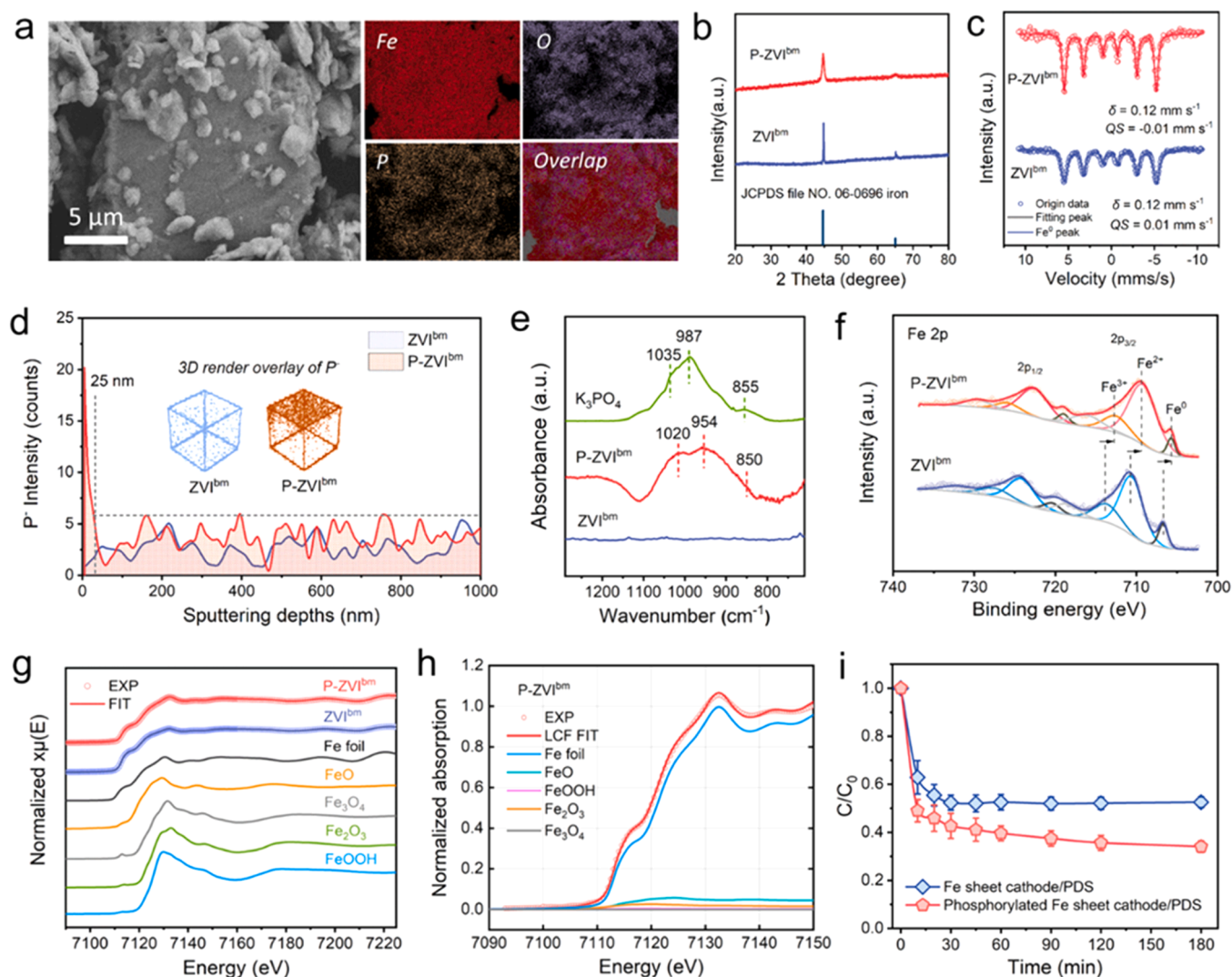


Fig. 2. Key active sites of PDS activation. (a) SEM and EDS mapping images of Fe, O and P elements for P-ZVI^{bm}. (b) XRD patterns of ZVI^{bm} and P-ZVI^{bm}. (c) ⁵⁷Fe Mössbauer spectra of ZVI^{bm} and P-ZVI^{bm}. (d) ToF-SIMS depth profiles of P in ZVI^{bm} and P-ZVI^{bm}, and the three-dimensional render overlay images (inset). (e) Attenuated total reflection Fourier transformed infrared (ATR-FTIR) spectra of different samples. (f) High-resolution Fe 2p XPS spectra of ZVI^{bm} and P-ZVI^{bm}. (g) Fe K-edge XANES spectra of ZVI^{bm} and P-ZVI^{bm} compared with relevant standard samples. (h) Linear combination fitting (LCF) analysis of Fe K-edge X-ray absorption near edge structure (XANES) for P-ZVI^{bm}. (i) 4-CP removal in electrochemical activation of PDS with different cathodes. Reaction conditions: [4-CP]₀ = 0.1 mmol L⁻¹, [PDS]₀ = 5 mmol L⁻¹, current density = 5 mA cm⁻², electrolyte [Na₂SO₄] = 25 mmol L⁻¹, pH_{ini} = 6.5.

instrument, while P-ZVI^{bm} possessed significant P⁺ signal, which enriched on the surface and faded drastically within the depth of ca. 25 nm. On the contrary, the ToF-SIMS depth profiles of Fe and O indicated that the thickness of iron oxide layer in P-ZVI^{bm} was about 1000 nm (Figure S14), therefore P was mostly adsorbed on the surface of iron oxide, which was intuitively displayed in 3D render overlay (inset of Fig. 2d). Besides, the peaks at 132.9 eV and 132.0 eV of P 2p X-ray photoelectron spectroscopy (XPS) were assigned to the binding energies of 2p_{1/2} and 2p_{3/2} of PO₄³⁻ (Figure S15) [40]. The significant red-shift of the P-O stretching vibration bands was observed in the solid attenuated total reflection Fourier transform infrared (ATR-FTIR) spectrum of P-ZVI^{bm}, in comparison with those of the K₃PO₄ solid (Fig. 2e). Meanwhile, the electron density of surface Fe atoms increased, as evidenced by the negative shift of binding energies for P-ZVI^{bm} in Fe 2p XPS spectra (Fig. 2f). These results revealed the inner-sphere coordination complexes formed between phosphate and surface Fe atoms in P-ZVI^{bm} [41]. Moreover, the chemical adsorbed phosphate exhibited a good stability, as evidenced by the negligible phosphorus leaching (0.0053 mg L⁻¹, Figure S4) during the P-ZVI^{bm}/PDS reaction.

The Fe 2p XPS results and the linear combination fitting (LCF)

analysis of Fe K-edge X-ray absorption near edge structure (XANES) analysis indicated that the ball milling process and the phosphate modification were conducive to the exposure of more surface ≡Fe²⁺ sites (Fig. 2g–h, Figure S16, Table S3 and Table S4), which commonly served as the adsorption sites of PDS and the electron donors. Moreover, significantly higher ≡Feⁿ⁺/≡Fe⁰ (n = 2 and 3) ratios were detected in the depth-etching XPS spectra of the used P-ZVI^{bm} than that of the used ZVI^{bm} (Figure S17), suggesting that phosphate modification was crucial to drive electron transfer from the iron core and achieving PCET activation of PDS. We could conclude that the two important roles of iron oxide surface were to anchor the phosphate proton relays sites, and to provide electron donor sites, which together constructed the PCET reaction platform.

Interestingly, the PCET platform fabricated by phosphate modification also finds its universality in electrochemical reduction systems to boost PDS activation and pollutants removal (Text S6). Fig. 3i showed that, using Fe sheet as working electrode, 47.4% of 4-CP could be removed in 3 h with a constant current density of 5 mA/cm² applied on the cathode in neutral media. After phosphate modification of Fe sheet, the removal efficiency of 4-CP increased to 65.9% under the same

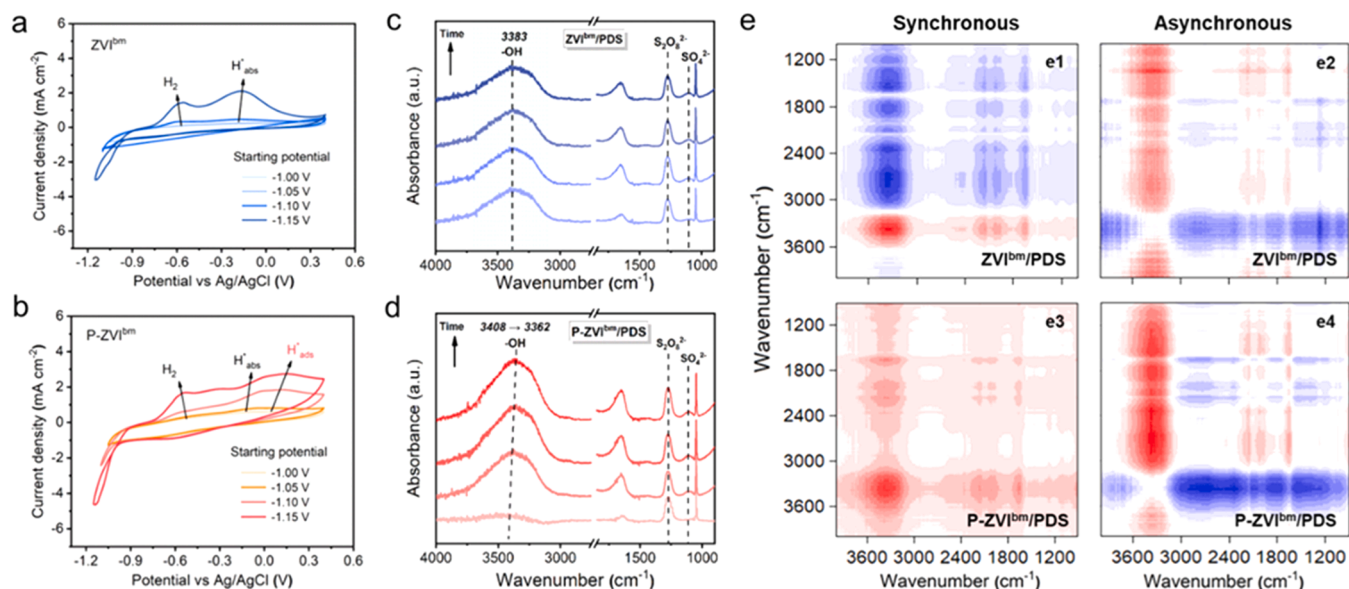


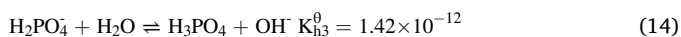
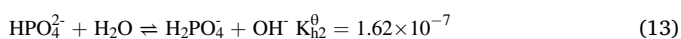
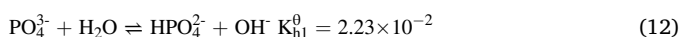
Fig. 3. Phosphate proton relay and hydrogen bond interaction during PCET. Electrochemical identification of various active hydrogen species in CVs scans with (a) ZVI^{bm} -coated and (b) P-ZVI^{bm} -coated glassy carbon electrode in deoxygenated $50 \text{ mmol L}^{-1} \text{ Na}_2\text{SO}_4$. *In-situ* ATR-FTIR spectra of (c) ZVI^{bm} (d) P-ZVI^{bm} during PDS activation. Reaction conditions: $[\text{PDS}]_0 = 20 \text{ mmol L}^{-1}$ (to obtain clearer spectra), $\text{pH}_{\text{ini}} = 4.0$. (e) 2D-COS synchronous and asynchronous spectra of ZVI^{bm} (e1, e2) and P-ZVI^{bm} (e3, e4) during PDS activation. The red and blue areas indicated the positive and negative intensities, respectively.

conditions. More importantly, the Fe ions leaching tests, D_2O solvent experiments, and control experiments demonstrated that the enhanced electrochemical activation of PDS was also driven by a similar PCET pathway mediated by electric field and surface-bound phosphate on the Fe cathode (Figure S18–S20).

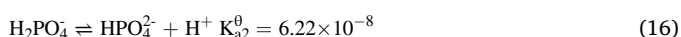
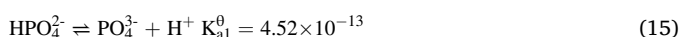
3.3. Phosphate proton relay and hydrogen bond interaction during PCET

On the basis of above results, we proposed that surface phosphate served as the proton relays, responsible for the surface inverse aggregate isotope effect of Z-sites on P-ZVI^{bm} , which accepted protons from the solvent (induction period) and subsequently donated the protons to the final acceptors to trigger the PCET activation of PDS (acceleration period). To confirm this assumption, we monitored the capacities of different samples to capture protons from the aqueous solution. ZVI^{bm} slightly increased the solution pH from 6.5 to 6.8, but P-ZVI^{bm} drastically escalated the solution pH to 7.8 (Figure S21), indicating the much stronger protonation of surface PO_4^{3-} (Eq. 12). The PCET activation of PDS requires the phosphate donating protons, but the equilibrium constant of HPO_4^{2-} deprotonation (Eq. 15, $K_{\text{a}1}^0$) is far below its protonation (Eq. 13, $K_{\text{h}2}^0$) [42]. Possibly when SO_4^{2-} oxidized H_2O (Eq. 17) to decrease the pH and generate H_2PO_4^+ with stronger proton donating ability (Figure S22–S23, Eqs. 14 and 16, $K_{\text{a}2}^0 \geq K_{\text{h}3}^0$), the PCET activation of PDS was accelerated.

Protonation:



Deprotonation:



After reaction of P-ZVI^{bm} /PDS, the binding energy of P 2p XPS spectrum of P-ZVI^{bm} shifted from 132.0 eV to 132.8 eV (Figure S24),

also in line with the protonation of surface PO_4^{3-} to H_2PO_4^+ in weak acid conditions. To confirm the important role of H^+ in the two periods, we also use the KH_2PO_4 , a polyprotic Brønsted acid that can directly provide pendant, as the modifier to prepare the $\text{HP-ZVI}^{\text{bm}}$ material. Figure S25 showed the comparisons of the 4-CP removal in the P-ZVI^{bm} /PDS and $\text{HP-ZVI}^{\text{bm}}$ /PDS systems at pH 6.5–10.5. Impressively, the 4-CP removal are quickly initiated in the $\text{HP-ZVI}^{\text{bm}}$ /PDS systems, and only one reaction stage was observed, which might be attributed to the presence of intrinsic protons on $\text{HP-ZVI}^{\text{bm}}$, without the need for the induction period to capture protons from the solvent.

It is still unclear how surface phosphate delivers phosphate protons (P-O-H) to the PDS molecules after its protonation. Notably, there was also protons (Fe-O-H) on the surface of ZVI^{bm} according to the fitting results of O 2p XPS spectra (Figure S26). But quite different from the Fe-O-H protons, the P-O-H protons were located in the second coordination sphere of surface Fe sites, also called “pendant protons”, with greater steric flexibility to facilitate their interaction with the PDS molecules (Figure S27). To certify the discrepancy of the surficial/interfacial proton types between two samples, cyclic voltammetry (CV) measurements were conducted. As displayed in Fig. 3, the oxidation peaks of H_2 (from -0.7 V to -0.5 V) and adsorbed H^*_{abs} (from -0.2 V to 0 V) were obtained in the curves of the ZVI^{bm} -coated electrode (Fig. 3a), whereas another oxidation peak at higher potential (from 0.1 V to 0.3 V) emerged in the CV of P-ZVI^{bm} -coated electrode (Fig. 3b), which was ascribed to adsorbed H^*_{ads} stemmed from the pendant protons of PO_4^{3-} groups [43].

We collected the time-resolved *in-situ* ATR-FTIR spectra to explore the interfacial interaction between the pendant protons and PDS molecules. During the ZVI^{bm} /PDS reaction, only the SO_4^{2-} vibration band at 1108 cm^{-1} increased (Fig. 3c). As for the P-ZVI^{bm} /PDS reaction, the $-\text{OH}$ stretching band significantly shifted from 3408 cm^{-1} to 3362 cm^{-1} (Fig. 3d), indicating the formation of interfacial hydrogen bond [44]. The ATR-FTIR spectra in Figs. 3c–3d were further transformed to two-dimensional correlation spectra (2D-COS), which could track the changing order of different chemical groups during the PDS activation (Fig. 3e). According to Nada’s rule (Text S7), the synchronous (Figure 3e1, e3) and asynchronous (Figure 3e2, e4) spectra indicated the sequence order of 3350 cm^{-1} ($-\text{OH}$) $>$ 1108 cm^{-1} (SO_4^{2-}) during the P-ZVI^{bm} /PDS reaction, suggesting that the protonation of P-ZVI^{bm} and

the hydrogen bond formation preceded the activation of PDS, in accordance with our assumption [45]. Whereas the sequence order for the ZVI^{bm}/PDS system was 1108 cm^{-1} (SO_4^{2-}) > 3350 cm^{-1} ($-\text{OH}$), indicating that PDS activation was independent on the hydroxylation of ZVI^{bm} surface. Therefore, the pendant protons of PO_4^{3-} groups could form hydrogen bonds with PDS, which may subsequently bridge the protons transfer from the PO_4^{3-} group to the O-O bond, triggering the PCET process to accelerate the simultaneous electron transfer for the O-O bond activation.

3.4. Theoretical study of PCET process in the P-ZVI^{bm}/PDS system

To fulfill the high-resolution vision of the PCET process during the P-ZVI^{bm}/PDS reaction, we performed theoretical study through DFT simulation (Text S8). The theoretical models of ZVI^{bm} and P-ZVI^{bm} were displayed in Figure S28. We first compared the adsorption energy of PDS on ZVI^{bm} and P-ZVI^{bm}. PDS chemically bounds to three Fe sites in a terminal end-on mode, by substituting three $-\text{OH}$ on ZVI^{bm}, with an adsorption energy of -0.95 eV , and the O-O bond marginally stretched from 1.489 \AA to 1.549 \AA (Fig. 4a). Marvelously, PDS is strongly adsorbed on the surface of P-ZVI^{bm} with a more negative adsorption energy of -2.67 eV , and the O-O bond significantly stretched to 2.136 \AA (Fig. 4b).

Unlike the $-\text{OH}$ fixed on the surface of ZVI^{bm}, the pendant proton (H_1) of PO_4^{3-} on P-ZVI^{bm} is more flexible and prone to interact with O_1 of the peroxide bond of the adsorbed PDS, experiencing an intermediate state (-3.57 eV) with the $\text{P}-\text{O}_3-\text{H}_1\cdots\text{O}_1$ hydrogen bond to the final state (-3.97 eV) where H_1 transfers from the $\text{P}-\text{O}_3-\text{H}_1$ to the O_1 atom, accompanied by the cleavage of O-O bond (Fig. 4c). This proton transfer and O-O bond activating process is barrierless, much more favorable than the PDS activation by ZVI^{bm} (activation barrier of $+1.53\text{ eV}$, Figure S29).

The electron donors of PDS activation were further verified by using the two-dimensional (2D) charge density difference slice map. The three surficial Fe atoms of ZVI^{bm} coordinating PDS (vertex positions of the dashed triangle) show stronger electron depletion, thus they donate electrons to the adsorbed PDS (Fig. 4d, left). In the P-ZVI^{bm}/PDS system, similar trend is obtained. Meanwhile, the Fe atom coordinated with phosphate (dashed circle) is charge-enriched after the PDS activation (Fig. 4d, right), so that the Fe atoms coordinated with PDS rather than that with phosphate donate electrons to PDS. Therefore, the PCET process of the P-ZVI^{bm}/PDS reaction is mediated by distinct donors of protons and electrons, respectively. Meanwhile, three-dimensional charge density difference analysis reveals that the PCET process significantly promotes the electron transfer from 0.82 eV to 1.52 eV (Fig. 4e).

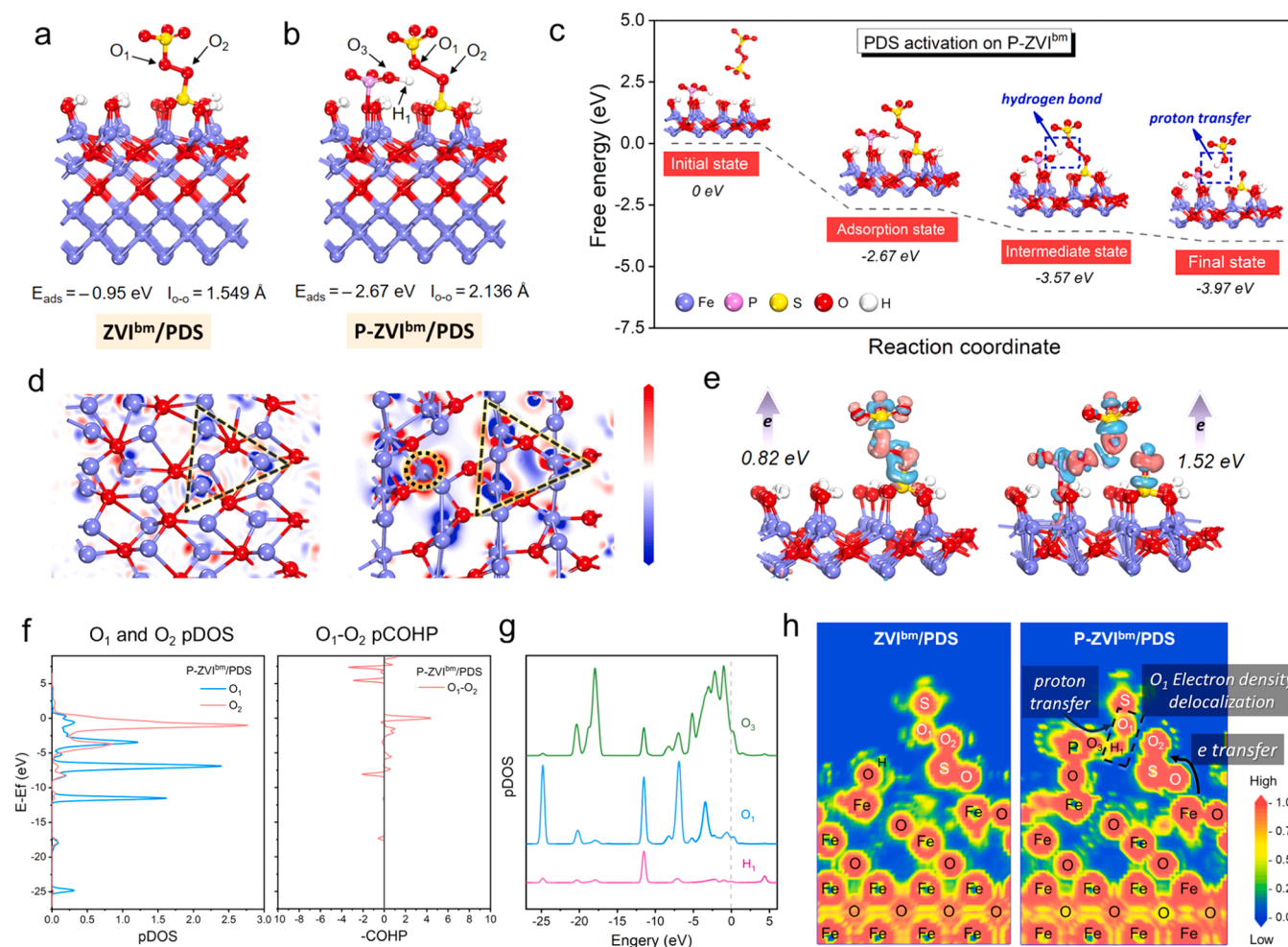


Fig. 4. Theoretical study of PCET process in the P-ZVI^{bm}/PDS system. Adsorption of PDS on the surface of (a) ZVI^{bm} and (b) P-ZVI^{bm}. (c) Free energy change during the adsorption and activation of PDS on the P-ZVI^{bm} surface. (d) Two-dimensional (2D) charge density difference slice map in the plane of PDS-coordinated Fe atoms for ZVI^{bm} (left) and P-ZVI^{bm} (right) after PDS activation. The red and blue slices depict charge accumulation and depletion in the space, respectively. (e) The charge density difference over ZVI^{bm} (left) and P-ZVI^{bm} (right) after PDS activation. The red and blue iso-surfaces depict charge accumulation and depletion in the space, respectively. (f) pDOS and pCOHP curves for O_1/O_2 and O_1-O_2 bond of PDS activated on the P-ZVI^{bm} surface, showing the density of states on certain atom or chemical bond as a function of energy relative to the Fermi level. (g) pDOS curves for H_1 , O_1 and O_3 of P-ZVI^{bm}/PDS, respectively. (h) The color-filled plane maps of EFL. The red and blue iso-surfaces depict electron accumulation and deficiency in the space, respectively.

We thus performed density of states (DOS) and crystal orbital Hamilton population (COHP) analysis to gather more detailed information of the PCET process. The free PDS has identical project DOS (pDOS) curves of O₁ and O₂, and the σ orbitals contribute significantly to the O₁-O₂ bond (Figure S30), suggesting that the O-O bond of PDS is symmetric and stable [46]. After being adsorbed on ZVI^{bm}, the molecular orbital of PDS rehybridizes with the metal bands, causing the differential pDOS curves of O₁ and O₂, as well as the uprising contribution of *p* orbitals to the molecular orbitals of O₁-O₂ bond (Figure S31), implying the polarization and reduced stability of the O₁-O₂ bond [47]. Intriguingly, when PDS is adsorbed on P-ZVI^{bm}, the bonding orbitals of O₁-O₂ bond strongly polarize toward O₂, inducing a highly asymmetric electron cloud distribution of the O₁-O₂ bond (Fig. 4f). The less negative integrated COHP (ICOHP) value also reflects the significantly destabilized O₁-O₂ bond of PDS on P-ZVI^{bm} (Table S5) [48]. Moreover, the antibonding orbitals below Fermi level are mainly filled by the electrons of O₁, suggesting the destabilization of O₁-O₂ bond by the electron cloud redistribution of O₁.

We further took the hydrogen bond (P-O₃-H₁...O₁) into consideration and investigated the orbital coupling of O₃, H₁ and O₁. As depicted in Fig. 4g, the orbital coupling between O₁ and H₁ is higher than that between O₃ and H₁, confirming the strong hydrogen bonding interaction between O₁ and H₁. Furthermore, the ICOHP values of O₃-H₁ bond increases from -1.13 to -0.86 after the PDS adsorption (Table S5), suggesting that O₃-H₁ bond is destabilized by the PDS adsorption. The pCOHP curve of O₃-H₁ bond also shows significant increase of the antibonding orbital population in the range of -10 eV to -5 eV (Figure S32), corresponding to the energy level of the highest electron density in the O₁ pDOS curve. These results reveal that the electron density delocalization of O₁ can transfer electrons to O₃-H₁ antibonding orbitals, thereby driving the hydrogen bond interaction between P-ZVI^{bm} and PDS. The local electronic states of a reaction intermediate state in two systems have been investigated from the perspective of the topological analysis of the electron localization function (ELF). As depicted as Fig. 4h, the electron density between O₁ and O₂ of the adsorbed PDS was significantly reduced after phosphorylation of ZVI, implying the weakened peroxy bond strength in P-ZVI^{bm}/PDS system. Impressively, in the P-ZVI^{bm}/PDS system, the electron density between H₁ and O₁ exhibited a high electron density distribution, which confirmed the strong coupling interactions between them.

On the basis of the above results and analysis, we conclude that the PDS activation with P-ZVI^{bm} experiences two main stages, including the initial induction stage that the protonation of surface PO₄³⁻ constructs a proton-enriched microenvironment at the interface, and the subsequent PCET acceleration stage. The resulting sterically flexible pendant proton (P-O₃-H₁) in first stage is transferred to the adsorbed PDS through a strong hydrogen bond (P-O₃-H₁...O₁) intermediate state owing to the strong orbital couplings between H₁ and O₁, thereby greatly triggering the electron density delocalization of O₁ and polarizing the O₁-O₂ bond, resulting in an energy-barrierless transfer of electron from the surface $\equiv\text{Fe}^{2+}$ sites to the coordinated PDS molecules, and a cleavage of the O₁-O₂ bond to produce highly reactive radical species.

4. Conclusion

Heterogeneous peroxydisulfate (PDS) activation to produce highly reactive species is one of the most appealing methods for environment remediation, but the O-O bond cleavage driven by conventional electron transfer is often confronted with high energetic barriers and sluggish kinetics. This is the first proton-coupled electron transfer (PCET) strategy to boost PDS activation. A PCET platform paradigm of phosphorylated zero-valent iron (ZVI) was fabricated with the facile ball-milling method, where ZVI, surface-bound phosphate, and solvent water served as the electron donor, the proton relay, and the proton donor, respectively. High performance of this phosphorylated zero-valent iron activating PDS system confirms the effectiveness of this PCET strategy, and

extends the new application of heterogeneous PCET reactions in the environmental field.

CRediT authorship contribution statement

Zhihui Ai: Writing – review & editing, Project administration, Funding acquisition. **Lizhi Zhang:** Writing – review & editing, Supervision, Funding acquisition, Conceptualization. **Chuan Liang:** Writing – original draft, Investigation, Formal analysis, Data curation. **Xiufan Liu:** Software, Formal analysis. **Cancan Ling:** Validation, Supervision. **Furong Guo:** Software, Methodology. **Meiqi Li:** Methodology. **Xiang Zhang:** Resources. **Yiyi Shu:** Validation. **Hongwei Sun:** Writing – review & editing, Formal analysis.

Declaration of Competing Interest

The authors declare that they have no known competing financial interests or personal relationships that could have appeared to influence the work reported in this paper.

Data Availability

Data will be made available on request.

Acknowledgements

This work was supported by the National Key Research and Development Program of China (2023YFC3708002), the National Natural Science Foundation of China (U20A20129, U22A20402, 21936003, 22276068, U21A2039, 22076061, and 22376076), the Fundamental Research Funds for the Central Universities (CCNU22JC013, CCNU22JC014), and Key Research and Development Program of Hubei Province (2023BCB103).

Appendix A. Supporting information

Supplementary data associated with this article can be found in the online version at doi:10.1016/j.apcatb.2024.124025.

References

- [1] B.C. Hodges, E.L. Cates, J.H. Kim, Challenges and prospects of advanced oxidation water treatment processes using catalytic nanomaterials, *Nat. Nanotechnol.* 13 (2018) 642–650.
- [2] Y.J. Zhang, J.J. Chen, G.X. Huang, W.W. Li, H.Q. Yu, M. Elimelech, Distinguishing homogeneous advanced oxidation processes in bulk water from heterogeneous surface reactions in organic oxidation, *Proc. Natl. Acad. Sci. U. S. A.* 120 (2023) e2302407120.
- [3] Y. Chen, G. Zhang, H. Liu, J. Qu, Confining free radicals in close vicinity to contaminants enables ultrafast Fenton-like processes in the interspacing of MoS₂ membranes, *Angew. Chem. Int. Ed.* 58 (2019) 8134–8138.
- [4] C. Song, Q. Zhan, F. Liu, C. Wang, H. Li, X. Wang, X. Guo, Y. Cheng, W. Sun, L. Wang, J. Qian, B. Pan, Overturned loading of inert CeO₂ to active Co₃O₄ for unusually improved catalytic activity in Fenton-like reactions, *Angew. Chem. Int. Ed.* 61 (2022) e202200406.
- [5] S. Zhu, X. Huang, F. Ma, L. Wang, X. Duan, S. Wang, Catalytic removal of aqueous contaminants on N-doped graphitic biochars: Inherent roles of adsorption and nonradical mechanisms, *Environ. Sci. Technol.* 52 (2018) 8649–8658.
- [6] S. Wacławek, H.V. Lutze, K. Grübel, V.V.T. Padil, M. Černík, D.D. Dionysiou, Chemistry of persulfates in water and wastewater treatment: a review, *Chem. Eng. J.* 330 (2017) 44–62.
- [7] J. Lee, U. von Gunten, J.H. Kim, Persulfate-based advanced oxidation: Critical assessment of opportunities and roadblocks, *Environ. Sci. Technol.* 54 (2020) 3064–3081.
- [8] Y. Yan, Z. Wei, X. Duan, M. Long, R. Spinney, D.D. Dionysiou, R. Xiao, P.J. Alvarez, Merits and limitations of radical vs. nonradical pathways in persulfate-based advanced oxidation processes, *Environ. Sci. Technol.* 57 (2023) 12153–12179.
- [9] X. Duan, C. Su, J. Miao, Y. Zhong, Z. Shao, S. Wang, H. Sun, Insights into perovskite-catalyzed peroxydisulfate activation: maneuverable cobalt sites for promoted evolution of sulfate radicals, *Appl. Catal. B* 220 (2018) 626–634.

- [10] Y. Gao, Y. Zhu, Z. Chen, Q. Zeng, C. Hu, Insights into the difference in metal-free activation of peroxymonosulfate and peroxydisulfate, *Chem. Eng. J.* 394 (2020) 123936.
- [11] J. Song, N. Hou, X. Liu, M. Antonietti, P. Zhang, R. Ding, L. Song, Y. Wang, Y. Mu, Asymmetrically coordinated CoB_3N_3 moieties for selective generation of high-valence Co-oxo species via coupled electron proton transfer in Fenton-like reactions, *Adv. Mater.* 35 (2023) 2209552.
- [12] R. Tyburski, T. Liu, S.D. Glover, L. Hammarström, Proton-coupled electron transfer guidelines, fair and square, *J. Am. Chem. Soc.* 143 (2021) 560–576.
- [13] R.G. Agarwal, S.C. Coste, B.D. Groff, A.M. Heuer, H. Noh, G.A. Parada, C.F. Wise, E. M. Nichols, J.J. Warren, J.M. Mayer, Free energies of proton-coupled electron transfer reagents and their applications, *Chem. Rev.* 122 (2022) 1–49.
- [14] Y. Zhang, H. Zhang, H. Ji, W. Ma, C. Chen, J. Zhao, Pivotal role and regulation of proton transfer in water oxidation on hematite photoanodes, *J. Am. Chem. Soc.* 138 (2016) 2705–2711.
- [15] Y. Zhang, H. Zhang, A. Liu, C. Chen, W. Song, J. Zhao, Rate-limiting O–O bond formation pathways for water oxidation on hematite photoanode, *J. Am. Chem. Soc.* 140 (2018) 3264–3269.
- [16] Z. Thammavongsy, I.P. Mercer, J.Y. Yang, Promoting proton coupled electron transfer in redox catalysts through molecular design, *Chem. Commun.* 55 (2019) 10342–10358.
- [17] J.C. Lennox, D.A. Kurtz, T. Huang, J.L. Dempsey, Excited-state proton-coupled electron transfer: different avenues for promoting proton/electron movement with solar photons, *ACS Energy Lett.* 2 (2017) 1246–1256.
- [18] D.K. Bediako, B.H. Solis, D.K. Dogutan, M.M. Roubelakis, A.G. Maher, C.H. Lee, M. B. Chambers, S. Hammes-Schiffer, D.G. Nocera, Role of pendant proton relays and proton-coupled electron transfer on the hydrogen evolution reaction by nickel hangman porphyrins, *Proc. Natl. Acad. Sci. U. S. A.* 111 (2014) 15001–15006.
- [19] G. Chen, T. Wang, P. Liu, Z. Liao, H. Zhong, G. Wang, P. Zhang, M. Yu, E. Zschech, M. Chen, J. Zhang, X. Feng, Promoted oxygen reduction kinetics on nitrogen-doped hierarchically porous carbon by engineering proton-feeding centers, *Energy Environ. Sci.* 13 (2020) 2849–2855.
- [20] C. Costentin, V. Hájí, M. Robert, J.M. Saveant, C. Tard, Concerted heavy-atom bond cleavage and proton and electron transfers illustrated by proton-assisted reductive cleavage of an O–O bond, *Proc. Natl. Acad. Sci. U. S. A.* 108 (2011) 8559–8564.
- [21] R.A. Marcus, Electron transfer reactions in chemistry theory and experiment, *J. Electroanal. Chem.* 438 (1997) 251–259.
- [22] D. Kiejza, U. Kotowska, W. Polńska, J. Karpińska, Peracids-new oxidants in advanced oxidation processes: the use of peracetic acid, peroxymonosulfate, and persulfate salts in the removal of organic micropollutants of emerging concern—a review, *Sci. Total Environ.* 790 (2021) 148195.
- [23] P.R. Bergethon, Which way is that system going? The gibbs free energy. The Physical basis of biochemistry: The Foundations of Molecular Biophysics, Springer New York, New York, NY, 2010, pp. 327–350.
- [24] L. Wang, L. Yang, L. Huang, D. Cao, Diketopyrrolopyrrole-derived Schiff base as colorimetric and fluorometric probe for sequential detection of HSO_4^- and Fe^{3+} with “off-on-off” response, *Sens. Actuators B Chem.* 209 (2015) 536–544.
- [25] K. Wei, H. Li, H. Gu, X. Liu, C. Ling, S. Cao, M. Li, M. Liao, X. Peng, Y. Shi, W. Shen, C. Liang, Z. Ai, L. Zhang, Strained zero-valent iron for highly efficient heavy metal removal, *Adv. Funct. Mater.* 32 (2022) 2200498.
- [26] M. Li, H. Shang, H. Li, Y. Hong, C. Ling, K. Wei, B. Zhou, C. Mao, Z. Ai, L. Zhang, Kirkendall effect boosts phosphorylated nZVI for efficient heavy metal wastewater treatment, *Angew. Chem. Int. Ed.* 60 (2021) 17115–17122.
- [27] L. Vilčiauskas, M.E. Tuckerman, G. Bester, S.J. Paddison, K.D. Kreuer, The mechanism of proton conduction in phosphoric acid, *Nat. Chem.* 4 (2012) 461–466.
- [28] H. Sheng, H. Ji, W. Ma, C. Chen, J. Zhao, Direct four-electron reduction of O_2 to H_2O on TiO_2 surfaces by pendant proton relay, *Angew. Chem. Int. Ed.* 52 (2013) 9686–9690.
- [29] Y. Mu, Z.H. Ai, L.Z. Zhang, Phosphate shifted oxygen reduction pathway on $\text{Fe@Fe}_2\text{O}_3$ core–shell nanowires for enhanced reactive oxygen species generation and aerobic 4-chlorophenol degradation, *Environ. Sci. Technol.* 51 (2017) 8101–8109.
- [30] Y.W. Pan, M.H. Zhou, Q. Wang, J.J. Cai, Y.S. Tian, Y. Zhang, EDTA, oxalate, and phosphate ions enhanced reactive oxygen species generation and sulfamethazine removal by zero-valent iron, *J. Hazard. Mater.* 391 (2020) 122210.
- [31] Q. Wang, Y.W. Pan, W.Y. Fu, H.Z. Wu, M.H. Zhou, Y. Zhang, Aminopolycarboxylic acids modified oxygen reduction by zero valent iron: proton-coupled electron transfer, role of iron ion and reactive oxidant generation, *J. Hazard. Mater.* 430 (2022) 128402.
- [32] X. Zhang, H.W. Sun, Y.B. Shi, C.C. Ling, M.Q. Li, C. Liang, F.L. Jia, X. Liu, L. Z. Zhang, Z.H. Ai, Oxalated zero valent iron enables highly efficient heterogeneous Fenton reaction by self-adapting pH and accelerating proton cycle, *Water Res.* 235 (2023) 119828.
- [33] William P. Fagan, Frederick A. Villamena, Jay L. Zweier, Linda K. Weavers, In situ EPR spin trapping and competition kinetics demonstrate temperature-dependent mechanisms of synergistic radical production by ultrasonically activated persulfate, *Environ. Sci. Technol.* 56 (2022) 3729–3738.
- [34] Z.S. Wei, Frederick A. Villamena, Linda K. Weavers, Kinetics and mechanism of ultrasonic activation of persulfate: an in situ EPR spin trapping study, *Environ. Sci. Technol.* 51 (2017) 3410–3417.
- [35] G.A. Parada, Z.K. Goldsmith, S. Kolmar, B. Pettersson Rimgard, B.Q. Mercado, L. Hammarström, S. Hammes-Schiffer, J.M. Mayer, Concerted proton-electron transfer reactions in the Marcus inverted region, *Science* 364 (2019) 471–475.
- [36] Y. Liu, C.C.L. McCrory, Modulating the mechanism of electrocatalytic CO_2 reduction by cobalt phthalocyanine through polymer coordination and encapsulation, *Nat. Commun.* 10 (2019) 1683.
- [37] J. Yu, Y. Qin, X. Wang, H. Zheng, K. Gao, H. Yang, L. Xie, Q. Hu, C. He, Boosting electrochemical nitrate-ammonia conversion via organic ligands-tuned proton transfer, *Nano Energy* 103 (2022) 107705.
- [38] S. Bae, R.N. Collins, T.D. Waite, K. Hanna, Advances in surface passivation of nanoscale zerovalent iron: a critical review, *Environ. Sci. Technol.* 52 (2018) 12010–12025.
- [39] L. Gong, X. Qiu, P.G. Tratnyek, C. Liu, F. He, $\text{FeN}_x(\text{C})$ -coated microscale zero-valent iron for fast and stable trichloroethylene dechlorination in both acidic and basic pH conditions, *Environ. Sci. Technol.* 55 (2021) 5393–5402.
- [40] J.F. Moulder, W.F. Stickle, W.M. Sobol, K.D. Bomben, *Handbook of X-Ray Photoelectron Spectroscopy*, 1992.
- [41] L. Wang, M. Cao, Z. Ai, L. Zhang, Dramatically enhanced aerobic atrazine degradation with $\text{Fe@Fe}_2\text{O}_3$ core–shell nanowires by tetrapolyphosphate, *Environ. Sci. Technol.* 48 (2014) 3354–3362.
- [42] CRC Handbook of Chemistry and Physics, 86th Edition Edited by David R. Lide (National Institute of Standards and Technology). *J. Am. Chem. Soc.* 128 (2006) 5585.
- [43] H. Zeng, G. Zhang, Q. Ji, H. Liu, X. Hua, H. Xia, M. Sillanpää, J. Qu, pH-independent production of hydroxyl radical from atomic H^+ -mediated electrocatalytic H_2O_2 reduction: A green Fenton process without byproducts, *Environ. Sci. Technol.* 54 (2020) 14725–14731.
- [44] H. Li, S. Chen, H. Shang, X. Wang, Z. Yang, Z. Ai, L. Zhang, Surface hydrogen bond network spatially confined BiOCl oxygen vacancy for photocatalysis, *Sci. Bull.* 65 (2020) 1916–1923.
- [45] I. Noda, Two-dimensional infrared spectroscopy, *J. Am. Chem. Soc.* 111 (1989) 8116–8118.
- [46] L. Lin, S. Yao, R. Gao, X. Liang, Q. Yu, Y. Deng, J. Liu, M. Peng, Z. Jiang, S. Li, Y. W. Li, X.D. Wen, W. Zhou, D. Ma, A highly CO-tolerant atomically dispersed Pt catalyst for chemoselective hydrogenation, *Nat. Nanotechnol.* 14 (2019) 354–361.
- [47] L. Poppa, C. Copéret, A. Comas-Vives, Increased back-bonding explains step-edge reactivity and particle size effect for CO activation on Ru nanoparticles, *J. Am. Chem. Soc.* 138 (2016) 16655–16668.
- [48] S. Maintz, V.L. Deringer, A.L. Tchougréeff, R. Dronskowski, LOBSTER: a tool to extract chemical bonding from plane-wave based DFT, *J. Comput. Chem.* 37 (2016) 1030–1035.